

## Article

# Improving the Performance of Solution–Processed Quantum Dot Light–Emitting Diodes via a HfO<sub>x</sub> Interfacial Layer

Jun Hyung Jeong <sup>1,2</sup>, Min Gye Kim <sup>1,2</sup>, Jin Hyun Ma <sup>1,2</sup>, Min Ho Park <sup>1,2</sup>, Hyoun Ji Ha <sup>1,2</sup>, Seong Jae Kang <sup>1,2</sup>, Min-Jae Maeng <sup>3</sup>, Young Duck Kim <sup>3,4</sup>, Yongsup Park <sup>3,4,\*</sup> and Seong Jun Kang <sup>1,2,\*</sup>

<sup>1</sup> Department of Advanced Materials Engineering for Information and Electronics, Kyung Hee University, Yongin 17101, Republic of Korea

<sup>2</sup> Integrated Education Program for Frontier Materials (BK21 Four), Kyung Hee University, Yongin 17104, Republic of Korea

<sup>3</sup> Department of Physics and Research Institute of Basic Sciences, Kyung Hee University, Seoul 02447, Republic of Korea

<sup>4</sup> Department of Information Display, Kyung Hee University, Seoul 02447, Republic of Korea

\* Correspondence: parky@khu.ac.kr (Y.P.); junkang@khu.ac.kr (S.J.K.)

**Abstract:** One of the major obstacles in the way of high–performance quantum dot light–emitting diodes (QLEDs) is the charge imbalance arising from more efficient electron injection into the emission layer than the hole injection. In previous studies, a balanced charge injection was often achieved by lowering the electron injection efficiency; however, high performance next–generation QLEDs require the hole injection efficiency to be enhanced to the level of electron injection efficiency. Here, we introduce a solution–processed HfO<sub>x</sub> layer for the enhanced hole injection efficiency. A large amount of oxygen vacancies in the HfO<sub>x</sub> films creates gap states that lower the hole injection barrier between the anode and the emission layer, resulting in enhanced light–emitting characteristics. The insertion of the HfO<sub>x</sub> layer increased the luminance of the device to 166,600 cd/m<sup>2</sup>, and the current efficiency and external quantum efficiency to 16.6 cd/A and 3.68%, respectively, compared with the values of 63,673 cd/m<sup>2</sup>, 7.37 cd/A, and 1.64% for the device without HfO<sub>x</sub> layer. The enhanced light–emitting characteristics of the device were elucidated by X–ray photoelectron, ultra–violet photoelectron, and UV–visible spectroscopy. Our results suggest that the insertion of the HfO<sub>x</sub> layer is a useful method for improving the light–emitting properties of QLEDs.

**Keywords:** quantum dots; light–emitting diodes; solution process



**Citation:** Jeong, J.H.; Kim, M.G.; Ma, J.H.; Park, M.H.; Ha, H.J.; Kang, S.J.; Maeng, M.-J.; Kim, Y.D.; Park, Y.; Kang, S.J. Improving the Performance of Solution–Processed Quantum Dot Light–Emitting Diodes via a HfO<sub>x</sub> Interfacial Layer. *Materials* **2022**, *15*, 8977. <https://doi.org/10.3390/ma15248977>

Academic Editor: Antonio Polimeni

Received: 1 December 2022

Accepted: 14 December 2022

Published: 15 December 2022

**Publisher’s Note:** MDPI stays neutral with regard to jurisdictional claims in published maps and institutional affiliations.



**Copyright:** © 2022 by the authors. Licensee MDPI, Basel, Switzerland. This article is an open access article distributed under the terms and conditions of the Creative Commons Attribution (CC BY) license (<https://creativecommons.org/licenses/by/4.0/>).

## 1. Introduction

Light–emitting diodes (LEDs) have been extensively researched in the past few decades as a component of electronic devices that have become indispensable for convenient human life. Various types of light–emitting materials, such as organics, perovskites, two–dimensional (2D) materials, and quantum dots (QDs) have been used to produce high brightness LEDs [1–4]. Among these light–emitting materials, QDs have been extensively emerging owing to their high color purity, solution processability, and facile tunable band gap [5,6].

Unfortunately, the brightness and efficiency of quantum dot light–emitting diodes (QLEDs) are not yet optimal and attempts were made to address these shortcomings by adjusting the charge imbalance between electron and hole injection [7–9]. The charge imbalance in QLEDs mainly originates from the presence of excess electrons and numerous studies have been conducted to resolve the problem. Recently, Jin et al. reported the inclusion of an organic electron–blocking layer (EBL) to rectify the charge balance by blocking the injection of electrons [10]. Zhang et al. reported the incorporation of a double–layered structure for electron transport to balance the charge injection [11].

Rather than restricting electron injection to balance the charge injection, another approach would be to improve the hole injection properties for high performance QLED devices. Accordingly, many efforts have been devoted to improve the hole injection characteristics of QLEDs, such as doping the hole injection layer (HIL) or hole transport layer (HTL). However, considering that the hole transporting characteristics are sensitively affected by the amount of dopant material, attaining efficient hole transporting characteristics with an undoped hole injection/transport layer continues to remain a challenge [12]. Attempts to subject the HIL or HTL to additional treatment have also been reported to improve the hole injection properties; however, this simultaneously complicated the device fabrication [13,14]. Therefore, introducing an additional anode buffer layer without doping or post-chemical treatment is necessary for obtaining solution-processed high performance QLEDs.

Here, we introduced a solution-processed  $\text{HfO}_x$  layer as an anode buffer layer to improve the performance of QLEDs. Although the  $\text{HfO}_x$  layer has been widely used as an insulating layer, modification thereof by introducing a large amount of defect states originating from the oxygen vacancies in the  $\text{HfO}_x$  film was expected to lower the hole injection barrier between the anode and emission layer. A large amount of oxygen vacancies was obtained via spin coating followed by thermally annealing the films at low temperature of 250 °C. The maximum luminance, external quantum efficiency, and current efficiency of the optimal device was 166,670  $\text{cd/m}^2$ , 3.68%, and 16.6  $\text{cd/A}$ , respectively. These quantities, which are representative of the QLEDs performance, are more than two-fold higher than those of the device without the  $\text{HfO}_x$  layer, indicating that the  $\text{HfO}_x$  layer efficiently enhanced the performance of the QLEDs.

## 2. Experimental Section

### 2.1. Solutions Preparation

Solutions of  $\text{HfO}_x$  with different concentrations were prepared by dissolving different amounts of  $\text{HfCl}_4$  (Sigma Aldrich, St. Louis, MO, USA) in 10 mL 2-methoxyethanol (Sigma Aldrich) to obtain 0.01, 0.03, and 0.05 M solution, after which the mixture was stirred for 30 min. A solution of vanadium oxide ( $\text{V}_2\text{O}_5$ ) was prepared by dissolving 0.1 mL of vanadium triisopropoxide oxide (Alfa Aesar, Massachusetts, USA) in 13 mL of isopropanol (IPA) in a nitrogen-filled glove box. After vigorously stirring the solution for 30 min, 66.5  $\mu\text{L}$  of deionized (DI) water was dropped into the solution to facilitate hydrolysis. A 1 wt% of Poly[(9,9-dioctylfluorenyl-2,7-diyl)-co-(4,4'-(4-sec-butylphenyl)diphenylamine)] (TFB) solution was prepared by dissolving TFB into *p*-xylene, followed by stirring at 80 °C for 30 min.

### 2.2. Device Fabrication

Patterned ITO glass was ultrasonicated with DI water, acetone, and IPA for 10 min. The substrates were dried in a stream of  $\text{N}_2$  gas, followed by exposure to UV-ozone for 15 min to render the surface hydrophilic and remove residual organics. Subsequently, the  $\text{HfO}_x$  solution was spin-coated onto the substrate at 3000 rpm for 30 s. The spin-coated  $\text{HfO}_x$  films were pre-annealed at 120 °C for 5 min to evaporate the solvents, and finally annealed at 250 °C for 45 min. After the coated substrate was allowed to cool, a  $\text{V}_2\text{O}_5$  solution was spin-coated onto the  $\text{HfO}_x$  layer at 3000 rpm for 30 s, followed by annealing at 60 °C for 5 min. Next, a solution of TFB, the HTL material, was spin-coated onto the  $\text{V}_2\text{O}_5$  layer at 3000 rpm for 30 s, followed by annealing at 180 °C for 30 min. Then, a solution of CdSe/ZnS QDs (Uniam, 20 mg/mL) was spin-coated onto the TFB layer at 2000 rpm for 30 s, followed by annealing at 100 °C for 10 min. The layer of QDs was covered with a layer of ZnO by spin coating a solution thereof (Avantama, N-10) onto the QDs at 2000 rpm for 30 s, followed by annealing at 100 °C for 10 min. Finally, an aluminum (Al) cathode (thickness: 130 nm) was thermally evaporated under vacuum ( $\sim 8 \times 10^{-6}$  Torr) at a rate of 3 Å/s using a metal shadow mask with an illuminating area of 4  $\text{mm}^2$ .

### 2.3. Characterization

The electroluminescence characteristics of the QLEDs were measured using an OLED I–V–L test system (M6100, McScience Inc., Suwon, Republic of Korea), which was equipped with a Keithley 2400 source meter and a Konica Minolta CS–2000 spectroradiometer. The ultra–violet photoelectron spectroscopy (UPS) measurements were performed at the Multi-dimensional Materials Research Center of Kyung Hee University using a helium discharge lamp (VG Scientific, photon energy 21.22 eV) in a custom–built ultra–high vacuum chamber (base pressure:  $5 \times 10^{-10}$  Torr). A sample bias of  $-10$  V was applied to determine the secondary electron cut–off (SECO) positions when the work function (WF) was measured. All spectra were recorded at room temperature by using a hemispherical analyzer (Scienta SES100, Uppsala, Sweden). The overall energy resolution was approximately 0.1 eV. X–ray photoelectron spectroscopy (XPS) measurements were conducted in an ultrahigh vacuum chamber ( $\sim 1 \times 10^{-9}$  Torr), using a spectrometer (Nexsa, Thermo Fisher Scientific, Massachusetts, USA) with an Al–K $\alpha$  (1486.6 eV) source. UV–visible measurements were conducted using a UV–vis spectrophotometer (Cary 100, Agilent, Santa Clara, USA) to acquire transmittance spectra of the layers. The surface morphology was investigated using AFM measurement (Dimension 3100 SPM, Bruker, Massachusetts, USA).

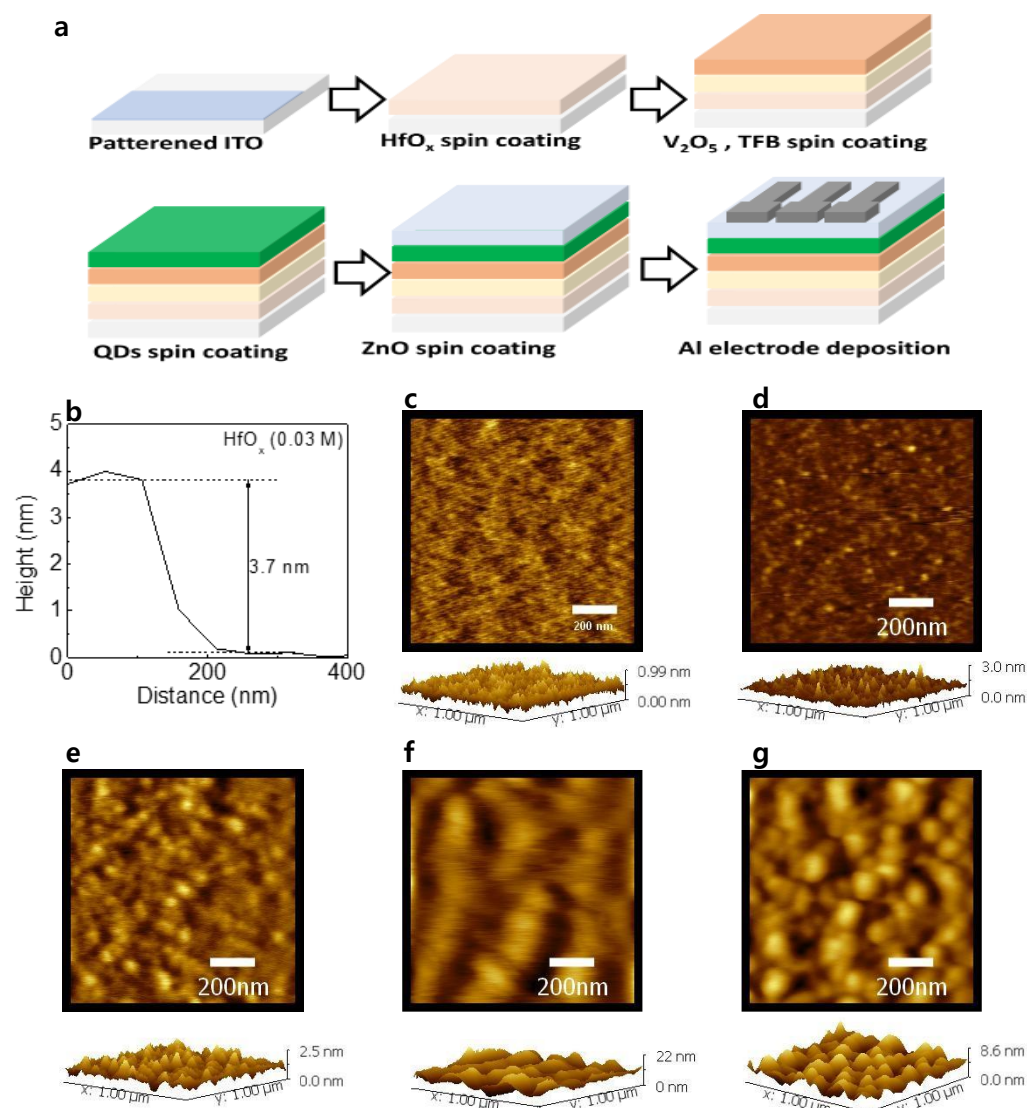
### 3. Results and Discussion

Figure 1a shows the schematic illustration of the device fabrication. The final structure of the device was ITO/(HfO<sub>x</sub>)/V<sub>2</sub>O<sub>5</sub>/TFB/QDs/ZnO/Al. Figure 1b shows the thickness of HfO<sub>x</sub> (0.03 M) film obtained from AFM measurement. The thickness was obtained to be 3.7 nm. The thickness of V<sub>2</sub>O<sub>5</sub>, TFB, QDs, and ZnO can be estimated to be 4.5, 12, 131, and 38 nm from our previous report [15]. Figure 1c–g shows the surface morphology and 3D topography of HfO<sub>x</sub> (0.03 M), V<sub>2</sub>O<sub>5</sub>, TFB, QD, and ZnO layers, respectively. The root mean square values of the layers were 0.1, 0.24, 0.31, 2.94, and 1.38 nm, respectively.

The UPS measurements were intended to determine the WF and valence band maximum (VBM) values of each of the layers from the SECO position and valence region. The SECO and valence region spectra of the ITO, ITO/HfO<sub>x</sub> (0.01 M), ITO/HfO<sub>x</sub> (0.03 M), and ITO/HfO<sub>x</sub> (0.05 M) films are shown in Figure 2a. The obtained WF values of ITO, and ITO/HfO<sub>x</sub> (0.01, 0.03, and 0.05 M) were 4.02, 4.07, 4.02, and 3.87 eV. The VBM values of HfO<sub>x</sub> (0.01, 0.03, and 0.05 M) were found to be 3.40, 3.41, and 3.39 eV, respectively. The SECO and valence region spectra of V<sub>2</sub>O<sub>5</sub>, HfO<sub>x</sub> (0.01 M)/V<sub>2</sub>O<sub>5</sub>, HfO<sub>x</sub> (0.03 M)/V<sub>2</sub>O<sub>5</sub>, and HfO<sub>x</sub> (0.05 M)/V<sub>2</sub>O<sub>5</sub> are shown in Figure 2b. The inset shows the near valence region spectra of each of the V<sub>2</sub>O<sub>5</sub> layers, indicating the gap states originating from the V<sup>4+</sup> state of V<sub>2</sub>O<sub>5</sub>, as previously reported [16–18]. The WF values of V<sub>2</sub>O<sub>5</sub> and those of the HfO<sub>x</sub> (0.01, 0.03, and 0.05 M)/V<sub>2</sub>O<sub>5</sub> layers were 4.94, 5.16, 5.24, and 5.17 eV, respectively. The VBM values of the V<sub>2</sub>O<sub>5</sub> layers were 2.55, 2.55, 2.52, and 2.53 eV, respectively, and the differences between the Fermi level ( $E_F$ ) and gap state were 0.63, 0.61, 0.59, and 0.62 eV, respectively. Figure 2c shows the optical band gaps of the HfO<sub>x</sub> films in the form of the Tauc plots derived from the UV–vis transmittance, using the following equation

$$\alpha h\nu = A(h\nu - E_g)^n \quad (1)$$

where  $\alpha$  is the absorption coefficient,  $h\nu$  is the photon energy,  $A$  is a constant,  $E_g$  is the optical band gap, and  $n = 1/2$  for a direct band gap semiconductor [19]. All the HfO<sub>x</sub> films had an optical band gap of 4.86 eV, regardless of the concentration of the HfO<sub>x</sub> solution. Figure 2d shows the optical band gaps of the V<sub>2</sub>O<sub>5</sub>, TFB, and QD layers of 2.67, 2.93, and 2.23 eV, respectively, derived from the Tauc plot. The optical transmission spectra, recorded by conducting UV–vis measurements of the V<sub>2</sub>O<sub>5</sub>/TFB/QDs/ZnO films with and without the HfO<sub>x</sub> layer, are shown in Figure 2e. All the films had high transmittance of more than 90% in the 520–580 nm region regardless of the presence of the HfO<sub>x</sub> layer, indicating that the HfO<sub>x</sub> films did not severely affect the transmittance of the device.



**Figure 1.** (a) Schematic illustration of the device fabrication. (b) Thickness of the HfO<sub>x</sub> (0.03 M) films obtained from AFM measurement. Surface morphology with 3D topography of (c) HfO<sub>x</sub> (0.03 M), (d) V<sub>2</sub>O<sub>5</sub>, (e) TFB, (f) QD, and (g) ZnO layers.

The chemical states of each of the layers in the device were examined in detail by using XPS to analyze for hafnium 4d (Hf 4d) and vanadium 2p (V 2p). Reliability was ensured by calibrating the binding energies by assigning the peak at 285 eV to C 1s. Figure 3a shows the Hf 4d spectra of the HfO<sub>x</sub> (0.01 M), HfO<sub>x</sub> (0.03 M), and HfO<sub>x</sub> (0.05 M) films. The doublet at binding energies of ~224.2 eV and 213.4 eV arose as a result of spin orbit splitting of the Hf 4d orbitals into Hf 4d<sub>3/2</sub> and Hf 4d<sub>5/2</sub>, respectively [20]. Figure 3b–d shows the Hf 4d<sub>3/2</sub> XPS results for the HfO<sub>x</sub> (0.01 M), HfO<sub>x</sub> (0.03 M), and HfO<sub>x</sub> (0.05 M) films, respectively. Because all the Hf 4d<sub>3/2</sub> peaks were slightly asymmetric, as shown in Figure 3b–d, Hf ions of different valences were considered to exist in the HfO<sub>x</sub> film. The XPS profile of Hf 4d<sub>3/2</sub> was deconvoluted into two peaks using Gaussian–Lorentzian fitting. The asymmetric Hf 4d<sub>3/2</sub> peak can be deconvoluted into two peaks centered at the binding energies of ~223.7 eV and ~225.1 eV. The Hf in HfO<sub>x</sub> is widely known to exist in the Hf<sup>4+</sup> and Hf<sup>x+</sup> (x < 4) states. The lower electronegativity of Hf (1.3) than oxygen (3.44) suggests that the Hf with lower valency (Hf<sup>x+</sup>), which would be less affected by the surrounding oxygen atoms, and would have lower binding energy than stoichiometric Hf in the form of HfO<sub>2</sub> [21]. This suggests that the amount of Hf<sup>x+</sup> is related to the amount of oxygen vacancies in the film, which is consistent with our previous report [22]. The



concentration of  $\text{Hf}^{x+}$  in  $\text{HfO}_x$  (0.01 M),  $\text{HfO}_x$  (0.03 M), and  $\text{HfO}_x$  (0.05 M) was 78.4, 80.7, and 79.5%, respectively, indicating that the  $\text{HfO}_x$  (0.03 M) film possesses the highest amount of oxygen vacancies.

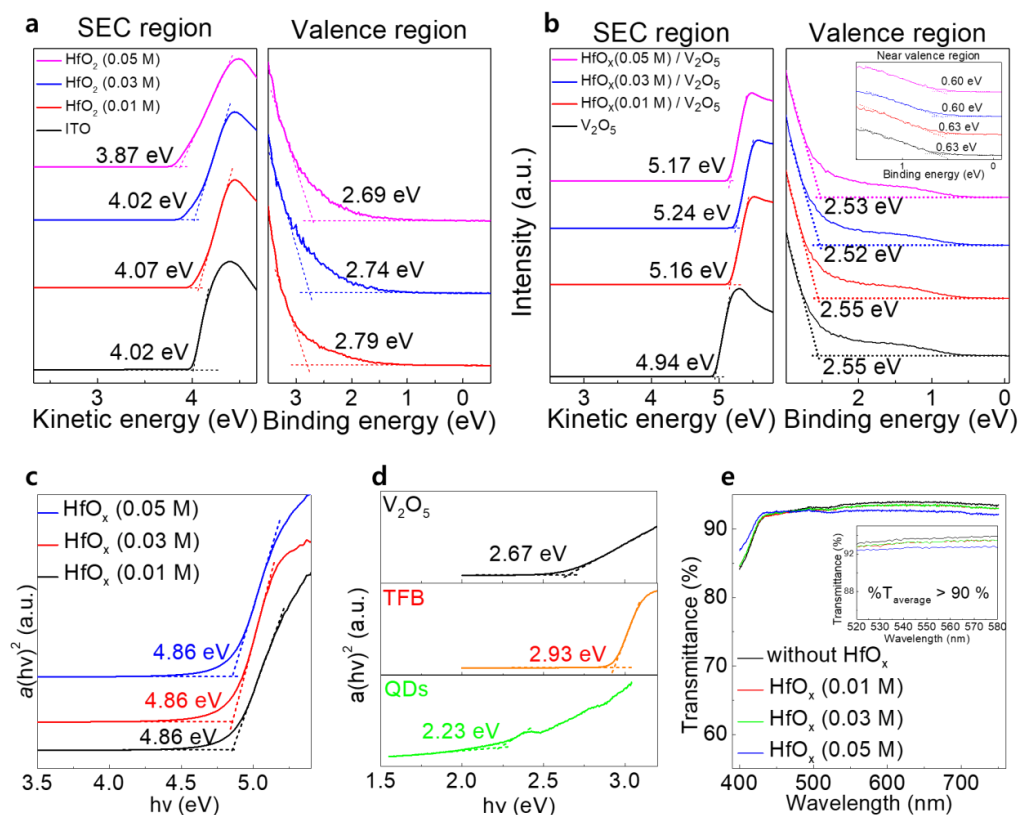


**Figure 2.** SEC and valence region spectra of (a) ITO,  $\text{HfO}_x$  (0.01 M),  $\text{HfO}_x$  (0.03 M), and  $\text{HfO}_x$  (0.05 M) films; and (b)  $\text{V}_2\text{O}_5$ ,  $\text{HfO}_x$  (0.01 M)/ $\text{V}_2\text{O}_5$ ,  $\text{HfO}_x$  (0.03 M)/ $\text{V}_2\text{O}_5$ , and  $\text{HfO}_x$  (0.05 M)/ $\text{V}_2\text{O}_5$  films. The inset shows the near valence region spectra of each of the films. Tauc plots of the (c)  $\text{HfO}_x$  (0.01 M),  $\text{HfO}_x$  (0.03 M), and  $\text{HfO}_x$  (0.05 M) films; and (d)  $\text{V}_2\text{O}_5$ , TFB, and QDs. (e) Optical transmittance spectra of glass/ $\text{V}_2\text{O}_5$ /TFB/QDs/ZnO films with and without the  $\text{HfO}_x$  layer.

figfig:materials-2102600-f004a–d shows the deconvoluted  $\text{V } 2p_{3/2}$  XPS profiles for the  $\text{V}_2\text{O}_5$ , and  $\text{HfO}_x$  (0.01, 0.03, and 0.05 M)/ $\text{V}_2\text{O}_5$  films, respectively. The  $\text{V } 2p_{3/2}$  spectrum was deconvoluted into two peaks centered at the higher and lower binding energies of  $\sim 517.7$  eV and  $\sim 516.6$  eV, respectively. The peak centered at the higher of these two values indicates the V in  $\text{V}^{5+}$ , whereas the peak centered at the lower value indicates the V in  $\text{V}^{4+}$  [23]. Because the  $\text{V}^{4+}$  state forms a hole transport channel near the Fermi level, it is necessary to clarify the concentration of  $\text{V}^{4+}$  in the  $\text{V}_2\text{O}_5$  film [16]. The concentration of  $\text{V}^{4+}$  in  $\text{V}_2\text{O}_5$ , and in the  $\text{HfO}_x$  (0.01, 0.03, and 0.05 M)/ $\text{V}_2\text{O}_5$  films was 23.13, 24.59, 26.00, and 25.49%; thus, the  $\text{HfO}_x$  (0.03 M)/ $\text{V}_2\text{O}_5$  film had the highest concentration of  $\text{V}^{4+}$ . During the formation of the  $\text{V}_2\text{O}_5$  layer above the oxygen-deficient  $\text{HfO}_x$  layer, the oxygen can diffuse from  $\text{V}_2\text{O}_5$  to  $\text{HfO}_x$  because of the difference in the oxygen density between  $\text{V}_2\text{O}_5$  and  $\text{HfO}_x$ . This indicates that the highest  $\text{V}^{4+}$  concentration of  $\text{HfO}_x$  (0.03 M)/ $\text{V}_2\text{O}_5$  could be the consequence of the existence of the highest concentration of oxygen vacancies in  $\text{HfO}_x$  (0.03 M) film [24].

figfig:materials-2102600-f005 shows the schematic interfacial energy band diagram of the QLEDs with the aligned Fermi level corresponding to the UPS results and the Tauc plot. The  $\text{V}^{4+}$ -related gap states of  $\text{V}_2\text{O}_5$  near the Fermi level are shown in Figure 5a–d. In the case of  $\text{HfO}_x$ , Hadacek et al. and Hildebrandt et al. reported that the oxygen-deficient  $\text{HfO}_x$  films exhibit  $p$ -type behavior. In addition, Kaiser et al. revealed that the origin of the  $p$ -type conductivity of oxygen-deficient  $\text{HfO}_x$  is due to the oxygen vacancy-related defect states, which are located  $\sim 3$  eV above the VBM [25–27]. Because of the high concen-

tration of  $\text{Hf}^{x+}$  in our  $\text{HfO}_x$  films representative of the large amount of oxygen vacancies in the  $\text{HfO}_x$  films, we indicated that the oxygen-related defect states of  $\text{HfO}_x$  are located 3 eV above the VBM. Therefore, as shown in Figure 5, all the devices containing the  $\text{HfO}_x$  layer would be expected to exhibit enhanced hole injection characteristics owing to the lowered hole injection barrier. In addition, because the device with the  $\text{HfO}_x$  (0.03 M) layer has the lowest hole injection barrier of 0.18 eV at the  $\text{HfO}_x/\text{V}_2\text{O}_5$  interface, the device with the  $\text{HfO}_x$  (0.03 M) layer would be predicted to exhibit the optimal hole injection characteristics.

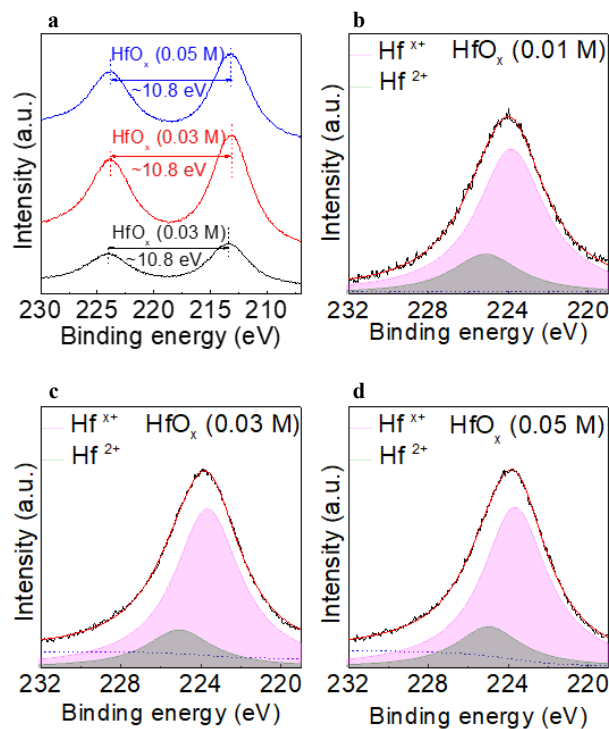


**Figure 3.** (a) Hf 4d spectra of  $\text{HfO}_x$  (0.01 M),  $\text{HfO}_x$  (0.03 M), and  $\text{HfO}_x$  (0.05 M) films. Deconvoluted Hf 4d<sub>3/2</sub> XPS profiles of the (b)  $\text{HfO}_x$  (0.01 M), (c)  $\text{HfO}_x$  (0.03 M), and (d)  $\text{HfO}_x$  (0.05 M) films.

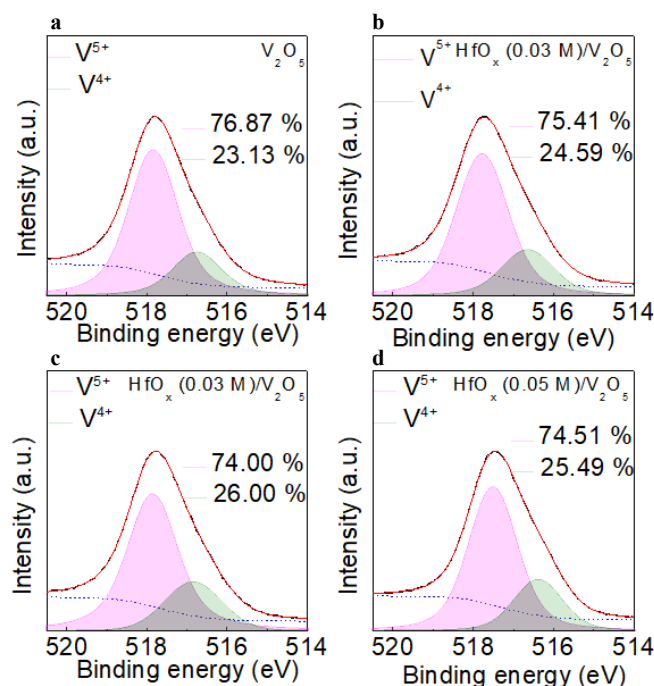


**Figure 4.** Deconvoluted V 2p<sub>3/2</sub> XPS results of the (a)  $\text{V}_2\text{O}_5$ , (b)  $\text{HfO}_x$  (0.01 M)/ $\text{V}_2\text{O}_5$ , (c)  $\text{HfO}_x$  (0.03 M)/ $\text{V}_2\text{O}_5$ , and (d)  $\text{HfO}_x$  (0.05 M)/ $\text{V}_2\text{O}_5$  films.

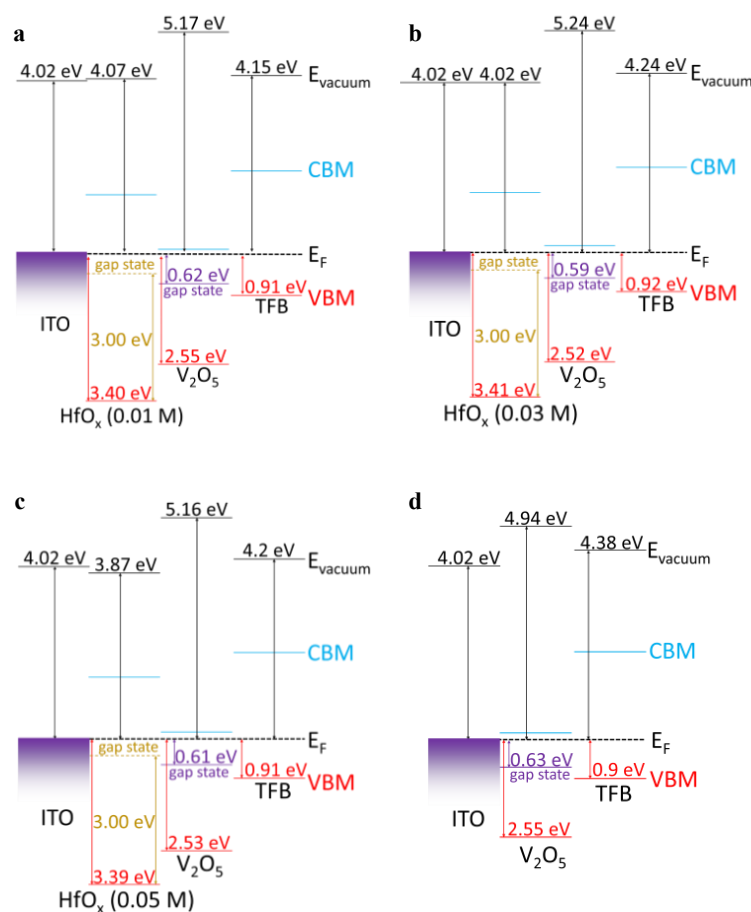


**Figure 5.** Schematic energy level diagram of QLEDs (a) without the  $\text{HfO}_x$  layer, and with the (b)  $\text{HfO}_x$  (0.01 M), (c)  $\text{HfO}_x$  (0.03 M), and (d)  $\text{HfO}_x$  (0.05 M) layer.

To corroborate the abovementioned results, we first recorded the current density–voltage ( $J$ – $V$ ) curves of the hole only devices (HODs) with the structure ITO/( $\text{HfO}_x$ )/ $\text{V}_2\text{O}_5$ /TFB/Al as shown in Figure 6a–b. The HOD without the  $\text{HfO}_x$  film had the lowest current density, with that of the  $\text{HfO}_x$  (0.01 M) film being slightly higher. The HOD with the  $\text{HfO}_x$  (0.03 M) film had the highest current density. Considering the alignment of the interfacial energy bands, as shown in Figure 5, the enhanced current density of the HOD can be attributed to the well–aligned gap states between the  $\text{HfO}_x$  and  $\text{V}_2\text{O}_5$  layers. Moreover, taking into account that the  $\text{HfO}_x$  (0.03 M)/ $\text{V}_2\text{O}_5$  film contains the highest concentration of gap states, originating from the  $\text{V}^{4+}$  state, the well–aligned energy levels and the concentration of gap states can both contribute to efficient hole injection. Figure 6c shows the current density–voltage–luminance ( $J$ – $V$ – $L$ ) characteristics of the QLEDs with and without the  $\text{HfO}_x$  (0.01, 0.03, and 0.05 M) layer. Consistent with the aforementioned improved hole injection characteristics, the QLED with the  $\text{HfO}_x$  (0.03 M) layer had the highest luminance of  $166,670 \text{ cd/m}^2$ , more than twice as high as the QLED without the  $\text{HfO}_x$  layer. In terms of the current density, the device without the  $\text{HfO}_x$  layer had higher values compared with the devices with the  $\text{HfO}_x$  layer. This can be attributed to the high conduction band offset between  $\text{HfO}_x$  and  $\text{V}_2\text{O}_5$ , which would have efficiently blocked the leakage current toward the ITO. Owing to the diminished leakage current and enhanced hole injection characteristics, the current efficiency (CE) and external quantum efficiency (EQE) of QLEDs with the  $\text{HfO}_x$  (0.03 M) layer increased considerably, as shown in Figure 6c,d. The device with the  $\text{HfO}_x$  (0.03 M) layer exhibited CE and EQE values of  $16.6 \text{ cd/A}$  and  $3.68\%$ , which is more than two–fold higher than the  $7.37 \text{ cd/A}$  and  $1.64\%$  of the device without the  $\text{HfO}_x$  layer. Figure 6e shows the electroluminescence (EL) spectra of the QLED devices with the  $\text{HfO}_x$  (0.01 M),  $\text{HfO}_x$  (0.03 M), and  $\text{HfO}_x$  (0.05 M) layers, and without the  $\text{HfO}_x$

layer at the maximum luminance of each of these devices. The operating image of the QLED is shown in the inset of Figure 6e. All the QLEDs had an emission peak with full width at half maximum (FWHM) of  $\sim 25$  nm without significant peak shift, indicating that the devices exhibited high color purity. To identify the stability of the device, the lifetime was confirmed at which the luminance reached half of the initial value with the initial luminance discussed, as shown in Figure 6f. The initial luminance values of the devices without  $\text{HfO}_x$  and with  $\text{HfO}_x$  (0.03 M) were 2320.2 and 2535.9  $\text{cd}/\text{m}^2$ , respectively. The lifetimes of the devices at an  $L_0 = 100 \text{ cd}/\text{m}^2$  was obtained using the following equation

$$(L_0)^n \times T_{50} = \text{constant} \quad (2)$$

where  $n$  is the acceleration factor (1.514),  $L_0$  is the initial luminance,  $L$  is the luminance, and  $T_{50}$  is the time which the luminance reached the half of the initial luminance value [22]. The longer lifetime of 139 h was obtained by adding  $\text{HfO}_x$  (0.03 M) layer, compared with the 75.9 h of the device without  $\text{HfO}_x$  layer.

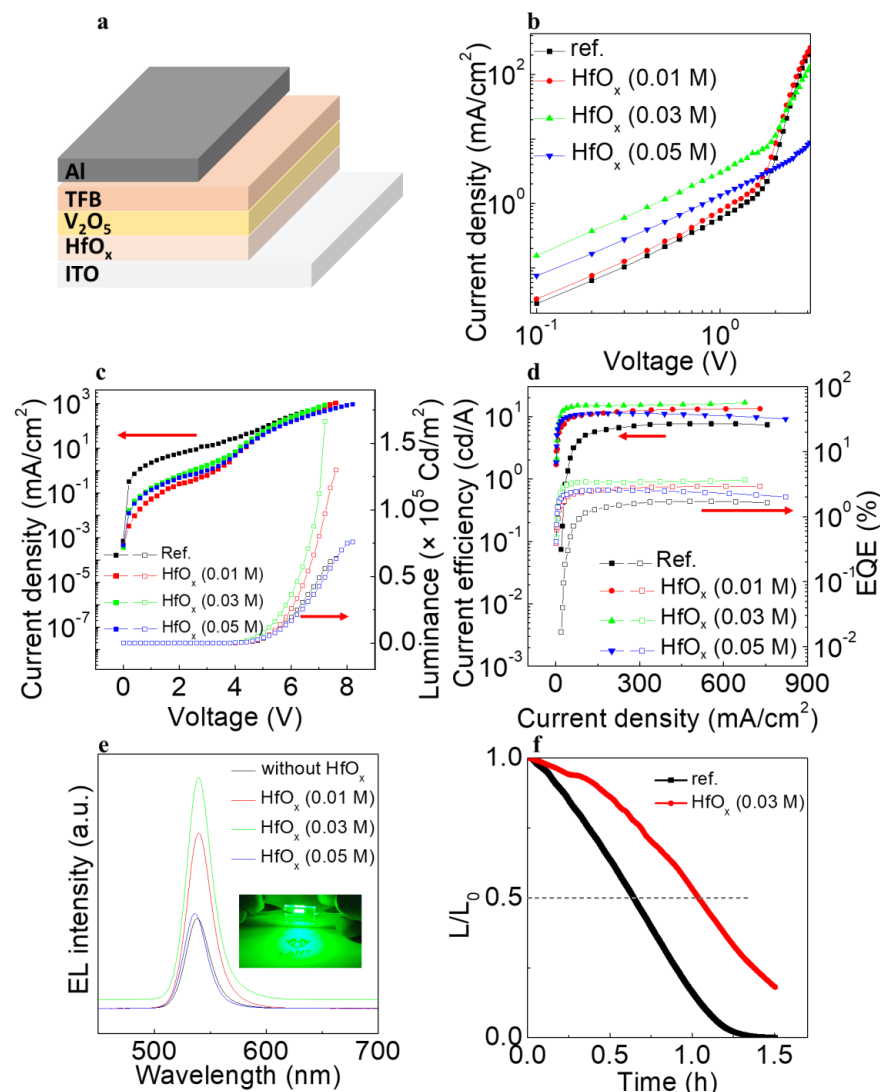


**Figure 6.** (a) Schematic illustration of the device fabrication process (b) J–V characteristics of HOD devices. (c) J–V–L characteristics and (d) current efficiency–current density plot of the QLED devices. (e) EL spectra of the QLED devices at each maximum luminance. (f) Lifetime data of the QLED devices without and with  $\text{HfO}_x$  (0.03 M) layer.



#### 4. Conclusions

We fabricated QLEDs with highly enhanced light-emitting characteristics by adding a solution-processed  $\text{HfO}_x$  interfacial layer. The defect states of the  $\text{HfO}_x$  layer, originating from the large amount of oxygen vacancies, could be well-aligned with the gap state of  $\text{V}_2\text{O}_5$ , resulting in lowering the hole injection barrier from ITO to  $\text{V}_2\text{O}_5$ . Furthermore, the oxygen-deficient  $\text{HfO}_x$  film also contributed to the increase in the formation of the  $\text{V}^{4+}$  state in the  $\text{V}_2\text{O}_5$  layer, resulting in enhanced hole injection characteristics. Owing to the improved hole injection characteristics, the device with the optimal  $\text{HfO}_x$  concentration had the highest luminance of  $166,670 \text{ cd/m}^2$ , current efficiency of  $16.6 \text{ cd/A}$ , and EQE of 3.68% compared with the values of  $63,673 \text{ cd/m}^2$ ,  $7.37 \text{ cd/A}$ , and 1.64%, respectively, for the device without  $\text{HfO}_x$  layer. UPS and XPS measurements enabled us to identify the origin of the enhanced light-emitting characteristics of the devices. Our results indicate that we developed a useful and facile method for improving the hole injection characteristics of QLEDs by incorporating a solution-processable  $\text{HfO}_x$  interfacial layer.

**Author Contributions:** J.H.J. and S.J.K. (Seong Jun Kang) planned the experimental details. J.H.J. contributed the fabrication of the devices and analyzing the measured data. M.-J.M., Y.P. and Y.D.K. contributed UPS measurement. M.G.K., J.H.M., H.J.H., M.H.P. and S.J.K. (Seong Jae Kang) conducted the experimental analysis. J.H.J. drafted the manuscript. S.J.K. (Seong Jun Kang) revised and confirmed the manuscript. All authors reviewed the manuscript. All authors have read and agreed to the published version of the manuscript.

**Funding:** This work was supported by a grant from Kyung Hee University (KHU-20181299).

**Institutional Review Board Statement:** Not applicable.

**Informed Consent Statement:** Not applicable.

**Data Availability Statement:** Data will be made available from the corresponding authors on reasonable request.

**Conflicts of Interest:** The authors declare no conflict of interest.

#### References

1. Moon, H.; Lee, C.; Lee, W.; Kim, J.; Chae, H. Stability of Quantum Dots, Quantum Dot Films, and Quantum Dot Light-Emitting Diodes for Display Applications. *Adv. Mater.* **2019**, *31*, 1804294. [\[CrossRef\]](#) [\[PubMed\]](#)
2. Zhang, L.; Sun, C.; He, T.; Jiang, Y.; Wei, J.; Huang, Y.; Yuan, M. High-Performance Quasi-2D Perovskite Light-Emitting Diodes: From Materials to Devices. *Light Sci. Appl.* **2021**, *10*, 61. [\[CrossRef\]](#) [\[PubMed\]](#)
3. Ji, K.; Anaya, M.; Abfalterer, A.; Stranks, S.D. Halide Perovskite Light-Emitting Diode Technologies. *Adv. Opt. Mater.* **2021**, *9*, 2002128. [\[CrossRef\]](#)
4. Sudheendran Swayamprabha, S.; Dubey, D.K.; Shah Nawaz; Yadav, R.A.K.; Nagar, M.R.; Sharma, A.; Tung, F.; Jou, J. Approaches for Long Lifetime Organic Light Emitting Diodes. *Adv. Sci.* **2020**, *8*, 2002254. [\[CrossRef\]](#)
5. Cheng, Y.; Wan, H.; Liang, T.; Liu, C.; Wu, M.; Hong, H.; Liu, K.; Shen, H. Continuously Graded Quantum Dots: Synthesis, Applications in Quantum Dot Light-Emitting Diodes, and Perspectives. *J. Phys. Chem. Lett.* **2021**, *12*, 5967–5978. [\[CrossRef\]](#)
6. Won, Y.-H.; Cho, O.; Kim, T.; Chung, D.-Y.; Kim, T.; Chung, H.; Jang, H.; Lee, J.; Kim, D.; Jang, E. Highly Efficient and Stable InP/ZnSe/ZnS Quantum Dot Light-Emitting Diodes. *Nature* **2019**, *575*, 634–638. [\[CrossRef\]](#)
7. Park, M.; Roh, J.; Lim, J.; Lee, H.; Lee, D. Double Metal Oxide Electron Transport Layers for Colloidal Quantum Dot Light-Emitting Diodes. *Nanomaterials* **2020**, *10*, 726. [\[CrossRef\]](#)
8. Jin, H.; Moon, H.; Lee, W.; Hwangbo, H.; Yong, S.H.; Chung, H.K.; Chae, H. Charge Balance Control of Quantum Dot Light Emitting Diodes with Atomic Layer Deposited Aluminum Oxide Interlayers. *RSC Adv.* **2019**, *9*, 11634–11640. [\[CrossRef\]](#)
9. Wang, F.; Sun, W.; Liu, P.; Wang, Z.; Zhang, J.; Wei, J.; Li, Y.; Hayat, T.; Alsaedi, A.; Tan, Z. Achieving Balanced Charge Injection of Blue Quantum Dot Light-Emitting Diodes through Transport Layer Doping Strategies. *J. Phys. Chem. Lett.* **2019**, *10*, 960–965. [\[CrossRef\]](#)
10. Jin, X.; Chang, C.; Zhao, W.; Huang, S.; Gu, X.; Zhang, Q.; Li, F.; Zhang, Y.; Li, Q. Balancing the Electron and Hole Transfer for Efficient Quantum Dot Light-Emitting Diodes by Employing a Versatile Organic Electron-Blocking Layer. *ACS Appl. Mater. Interfaces* **2018**, *10*, 15803–15811. [\[CrossRef\]](#)
11. Zhang, N.; Qu, X.; Lyu, Q.; Wang, K.; Sun, X.W. Highly Efficient Transparent Quantum-Dot Light-Emitting Diodes Based on Inorganic Double Electron-Transport Layers. *Photonics Res.* **2021**, *9*, 1979–1983. [\[CrossRef\]](#)

12. Sun, Y.; Chen, W.; Wu, Y.; He, Z.; Zhang, S.; Chen, S. A Low-Temperature-Annealed and UV-Ozone-Enhanced Combustion Derived Nickel Oxide Hole Injection Layer for Flexible Quantum Dot Light-Emitting Diodes. *Nanoscale* **2019**, *11*, 1021–1028. [[CrossRef](#)] [[PubMed](#)]
13. Dhar, S.; Chakraborty, P.; Majumder, T.; Mondal, S.P. Acid-Treated PEDOT:PSS Polymer and TiO<sub>2</sub> Nanorod Schottky Junction Ultraviolet Photodetectors with Ultrahigh External Quantum Efficiency, Detectivity, and Responsivity. *ACS Appl. Mater. Interfaces* **2018**, *10*, 41618–41626. [[CrossRef](#)] [[PubMed](#)]
14. Lee, J.H.; Jeong, Y.R.; Lee, G.; Jin, S.W.; Lee, Y.H.; Hong, S.Y.; Park, H.; Kim, J.W.; Lee, S.-S.; Ha, J.S. Highly Conductive, Stretchable, and Transparent PEDOT:PSS Electrodes Fabricated with Triblock Copolymer Additives and Acid Treatment. *ACS Appl. Mater. Interfaces* **2018**, *10*, 28027–28035. [[CrossRef](#)] [[PubMed](#)]
15. Shin, J.S.; Kim, M.; Ma, J.H.; Jeong, J.H.; Hwang, H.W.; Kim, J.W.; Kang, S.J. Solution-processable Li-doped transition metal oxide hole-injection layer for highly efficient quantum-dot light-emitting diodes. *J. Mater. Chem. C* **2022**, *10*, 5590–5597. [[CrossRef](#)]
16. Heo, S.B.; Yu, J.H.; Shin, J.S.; Kim, T.Y.; Kim, B.S.; Jeon, W.; Kang, S.J. Effect of Inorganic Interfacial Modification Layer on the Performance of Quantum-Dots Light-Emitting Diodes. *Jpn. J. Appl. Phys.* **2020**, *59*, 124002. [[CrossRef](#)]
17. Shin, J.S.; Kim, T.Y.; Heo, S.B.; Hong, J.-A.; Park, Y.; Kang, S.J. Improving the Performance of Quantum-Dot Light-Emitting Diodes via an Organic-Inorganic Hybrid Hole Injection Layer. *RSC Adv.* **2021**, *11*, 4168–4172. [[CrossRef](#)]
18. Kim, T.Y.; Park, S.; Kim, B.J.; Heo, S.B.; Yu, J.H.; Shin, J.S.; Hong, J.-A.; Kim, B.-S.; Kim, Y.D.; Park, Y.; et al. Dual-Functional Quantum-Dots Light Emitting Diodes Based on Solution Processable Vanadium Oxide Hole Injection Layer. *Sci. Rep.* **2021**, *11*, 1700. [[CrossRef](#)]
19. Park, S.; Kim, B.J.; Kang, S.J.; Cho, N.-K. Photocurrent Characteristics of Zinc-Oxide Films Prepared by Using Sputtering and Spin-Coating Methods. *J. Korean Phys. Soc.* **2018**, *73*, 1351–1355. [[CrossRef](#)]
20. Selvakumar, N.; Barshilia, H.C.; Rajam, K.S.; Biswas, A. Structure, Optical Properties and Thermal Stability of Pulsed Sputter Deposited High Temperature HfO<sub>x</sub>/Mo/HfO<sub>2</sub> Solar Selective Absorbers. *Sol. Energy Mater. Sol. Cells* **2010**, *94*, 1412–1420. [[CrossRef](#)]
21. Paul, A.D.; Biswas, S.; Das, P.; Edwards, H.J.; Dalal, A.; Maji, S.; Dhanak, V.R.; Mondal, A.; Mahapatra, R. Improved Resistive Switching Characteristics of Ag/Al:HfO<sub>x</sub>/ITO/PET ReRAM for Flexible Electronics Application. *Semicond. Sci. Technol.* **2021**, *36*, 065006. [[CrossRef](#)]
22. Kim, M.G.; Shin, J.S.; Ma, J.H.; Jeong, J.H.; Han, D.H.; Kim, B.-S.; Jeon, W.; Park, Y.; Kang, S.J. An Al-Doped TiO<sub>2</sub> Interfacial Layer for Effective Hole Injection Characteristics of Quantum-Dot Light-Emitting Diodes. *J. Mater. Chem. C* **2022**, *10*, 7294–7303. [[CrossRef](#)]
23. Narayanan, R.; Dewan, A.; Chakraborty, D. Complimentary Effects of Annealing Temperature on Optimal Tuning of Functionalized Carbon-V<sub>2</sub>O<sub>5</sub> Hybrid Nanobelts for Targeted Dual Applications in Electrochromic and Supercapacitor Devices. *RSC Adv.* **2018**, *8*, 8596–8606. [[CrossRef](#)] [[PubMed](#)]
24. Kita, K.; Toriumi, A. Origin of Electric Dipoles Formed at High-k/SiO<sub>2</sub> Interface. *Appl. Phys. Lett.* **2009**, *94*, 132902. [[CrossRef](#)]
25. Hadacek, N.; Nosov, A.; Ranno, L.; Strobel, P.; Galéra, R.-M. Magnetic Properties of HfO<sub>2</sub> Thin Films. *J. Phys. Condens. Matter* **2007**, *19*, 486206. [[CrossRef](#)]
26. Hildebrandt, E.; Kurian, J.; Müller, M.M.; Schroeder, T.; Kleebe, H.-J.; Alff, L. Controlled Oxygen Vacancy Induced *p*-Type Conductivity in HfO<sub>2-x</sub> Thin Films. *Appl. Phys. Lett.* **2011**, *99*, 112902. [[CrossRef](#)]
27. Kaiser, N.; Vogel, T.; Zintler, A.; Petzold, S.; Arzumanov, A.; Piro, E.; Eilhardt, R.; Molina-Luna, L.; Alff, L. Defect-Stabilized Substoichiometric Polymorphs of Hafnium Oxide with Semiconducting Properties. *ACS Appl. Mater. Interfaces* **2021**, *14*, 1290–1303. [[CrossRef](#)]